Journal of Alloys and Compounds 1010 (2025) 177195

Contents lists available at ScienceDirect

Journal of Alloys and Compounds

journal homepage: www.elsevier.com/locate/jalcom

Microstructure development and strengthening behaviour in hot-extruded Ti-Mo alloys with exceptional strength-ductility balance

Jeff Huang [a,b,*], Abdollah Bahador [a,c], Katsuyoshi Kondoh [a,*]

[a] Joining and Welding Research Institute, Osaka University, 11-1 Mihogaoka, Ibaraki, Osaka 567-0047, Japan
[b] Graduate School of Engineering, Osaka University, 2-1 Yamadaoka, Suita, Osaka 565-0871, Japan
[c] Materials Processing Institute, Eston Road, Middlesbrough TS6 6US, UK

ARTICLE INFO

Keywords:
Titanium alloys
Thermomechanical processing
Microstructure
Mechanical properties
Strengthening mechanisms

ABSTRACT

A series of strong and ductile Ti-Mo alloys containing 2.5, 5, 7.5 and 10 wt% Mo was experimentally investigated by a two-stage blended-elemental powder metallurgy process. This process consisted of a spark plasma sintering stage for powder-consolidation and in-situ-homogenisation, and a hot extrusion stage for densification and microstructure enhancement. Microstructures in the extruded alloys changed from α dominant to β dominant with molybdenum addition. Simultaneously, a grain refinement effect was observed due to suppressed α precipitation and increase β retention. A significant strengthening effect was observed with molybdenum addition. In comparison with similarly processed commercially pure titanium, Ti-10Mo exhibited a yield strength improvement of 290 % to 1382.8 MPa, and an ultimate tensile strength improvement of 239 % to 1496.5 MPa. Meanwhile, Ti-5Mo exhibited a yield strength improvement of 211 % (1007.9 MPa) without any substantial reduction in ductility, resulting in an exceptional tensile toughness of 361.3 $MJ.m^{-3}$. A quantitative analysis of strengthening mechanisms reveals considerable strengthening effects from solid solution strengthening, dislocation strengthening, and grain refinement effects. These factors arise from the novel multi-modal microstructures formed by thermomechanical processing at super-transus temperatures. The newly achieved balance of strength and ductility appears to be unrivalled amongst all previously reported binary Ti-Mo alloys.

1. Introduction

Titanium (Ti) and its alloys are a versatile class of lightweight materials with properties that are highly attractive for applications that demand high specific strengths, excellent chemical resistance and superior biocompatibility. At present, much of the Ti market remains cornered by the widespread Ti-6Al-4V alloy and the various grades of commercially pure (CP) Ti, which are well entrenched due to the maturity of their manufacturing infrastructure. However, Ti-6Al-4V leaves much to be desired due to the cost and strategic issues with vanadium (V) supply chains [1], as well as persistent concerns about its cyto-toxic effects in biomedical implants [2]. Meanwhile, CP-Ti often fails to provide adequate strengths to outcompete structural aluminium alloys and steels [3]. These drawbacks are major shortcomings amidst a rising demand for light alloys in the rapidly advancing transportation and biomedical technology sectors. Accordingly, the topics of Ti alloy design and complimentary processing technologies have attracted immense research interest in recent years. In these efforts, significant progress has been made towards reducing cost [4], improving performance as biomaterials [5,6], and optimization for newer manufacturing technologies such as powder metallurgy (PM) and additive manufacturing (AM) [7,8]. Collectively, these various developments greatly diversify the available compositions of titanium, which simultaneously broadens applications, and improves supply chain resilience and stability [9].

In close synergy with these trends, molybdenum (Mo) appears to be an attractive candidate as a relatively cost-effective and biocompatible substitute for V in stabilizing the high-temperature β-phase for alloy design purposes. As one of the cheapest isomorphous β-stabilizers, Mo provides some degree of cost benefit over V, while avoiding the processibility and stability issues brought on by cheaper intermetallic-forming β-stabilizers like iron (Fe) or manganese (Mn). The fundamentals of the Ti-Mo system were comprehensively explored in the early days of titanium development [10], however interest gradually waned due to processing limitations from the large difference in melting point between Mo (2623°C) and Ti (1668°C). This large melting point

* Corresponding authors at: Joining and Welding Research Institute, Osaka University, 11-1 Mihogaoka, Ibaraki, Osaka 567-0047, Japan.
E-mail addresses: huang.jeff.l9c@ecs.osaka-u.ac.jp (J. Huang), kondoh.katsuyoshi.jwri@osaka-u.ac.jp (K. Kondoh).

https://doi.org/10.1016/j.jallcom.2024.177195
Received 18 August 2024; Received in revised form 6 October 2024; Accepted 21 October 2024
Available online 22 October 2024

discrepancy presents severe technical and cost challenges in conventional casting processes and has traditionally limited the economic viability of the Ti-Mo system to a few specialized biomedical applications. However, with the recent maturity of PM as an effective means of solid-state alloying from pre-mixed powders, there has been some renewed interest in Ti-Mo alloys in the past decade [11–15]. While extensive investigations of the structural properties remain relatively sparse, a few studies have demonstrated acceptable strengths in binary Ti-Mo alloys prepared by PM [16,17]. The best performance thus far has been reported by Liang et. al, with gigapascal strengths and fracture strains of around 10 % in a harmonically structured Ti-10Mo alloy prepared by a sintering, diffusion treatment, and annealing process [16]. However, despite their high strength, the ductility of these alloys still fall short of the 40 % achieved in some hot forged castings of Ti-Mo [18,19], leaving substantial room for improvement in the technical process.

Hot-forging, and other thermomechanical processing (TMP) methods are an attractive means of improving the mechanical properties of both PM and cast alloys [20,21]. In addition to the classical benefits of microstructure and property control, TMP of PM alloys also serves to improve the density of sintered compacts. In the processing of Ti alloys containing slow diffusers such as rhenium (Re), tungsten (W), tantalum (Ta) and Mo, this is a powerful means of combatting Kirkendall porosity and other defects which potentially detract from the mechanical properties of PM alloys [22]. With the objective of attaining superior properties from PM based Ti-Mo alloys, we herein investigate the microstructure development and strengthening mechanisms in a series of strong and ductile Ti-Mo alloys with 2.5, 5, 7.5 and 10 wt% Mo. To the best of our knowledge, the combined sintering and extrusion approach produced exceptional strength-ductility balance that is superior to all prior reports of binary Ti-Mo alloys produced by other methods.

2. Materials and methods

2.1. Sample preparation

Hydride-dehydride (HDH) Ti powder (D_{50} = 31 μm, Toho Technical Service, Fig. 1a) was mixed with 2.5, 5, 7.5 and 10 wt% of fine Mo powder (D_{50} = 3 μm, Kojundo Chemical, Fig. 1b) by rotary ball mill (AV-2, Asahi-Rika) to prepare partially alloyed powder mixtures. To promote embedding of Mo particles on to the surfaces of the larger Ti grains, ZrO_2 balls of 10 mm diameter were included as milling media at a powder to ball ratio of 4:1. Each composition was milled for 6 h at a rotation speed of 90 rpm. After mixing, the partially alloyed powders were consolidated into fully alloyed billets by spark-plasma-sintering (SPS, SPS-1030S, SPS Syntex) using a graphite die of 42 mm diameter. For sintering, each sample was heated to 1100°C at a rate of 20°C.min^{-1} under a uniaxial

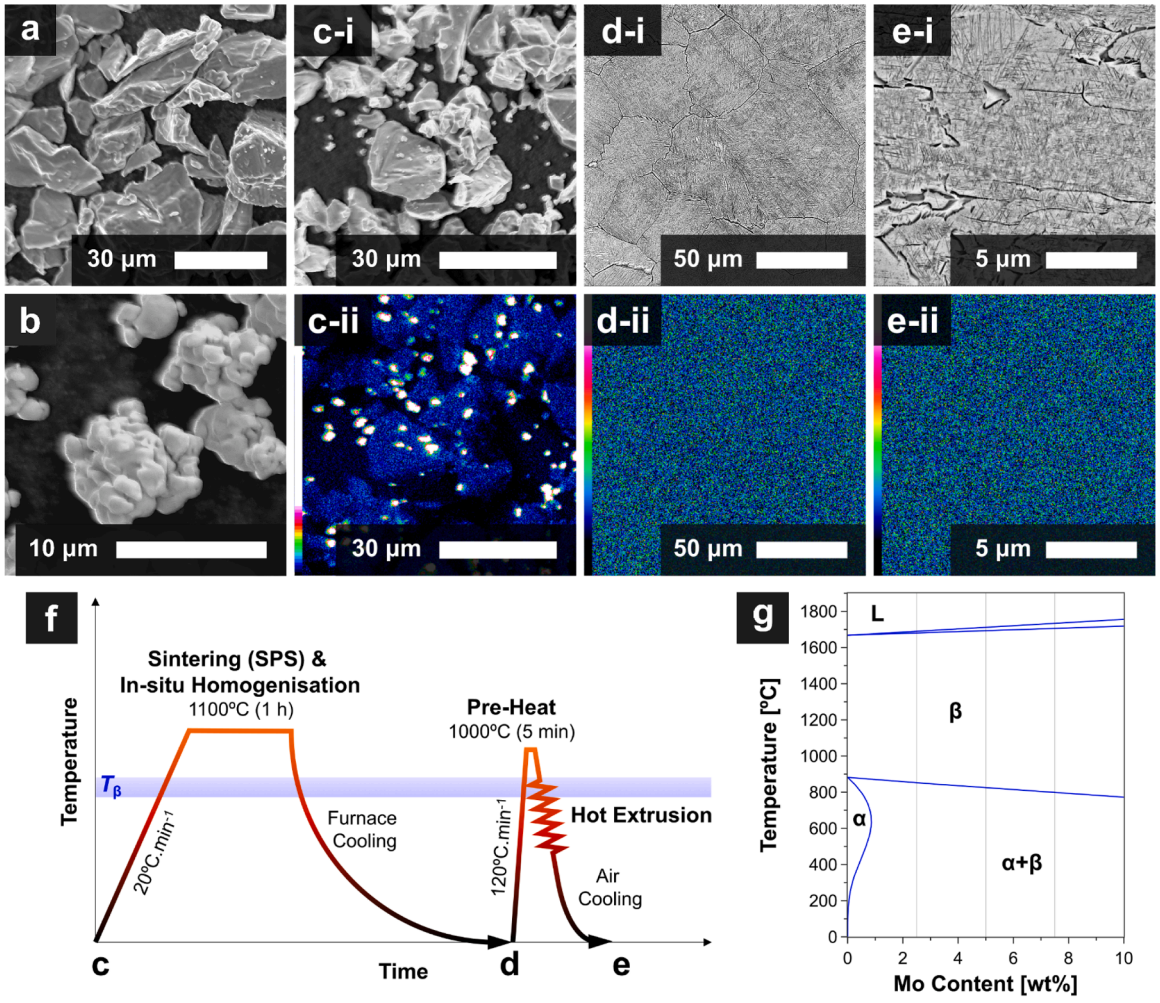

Fig. 1. Morphologies of as-received (a) HDH CP-Ti powder and (b) granular Mo powder. (c) Partially alloyed Ti-10Mo mixture after 6 h of rotary ball milling at 90 rpm, as observed by (-i) secondary electron imaging and (-ii) Mo elemental maps obtained by energy dispersive spectroscopy. (d) As-sintered, and (e) as-extruded microstructures produced from powder shown in (c), as observed in (-i) back-scattered electron imaging, and (-ii) Mo elemental maps. (f) Schematic showing the thermal history of the process used in this study. (g) Binary Ti-Mo phase diagram of the investigated composition range, calculated by the CompuTherm Pandat software [23].

compacting pressure of 15 MPa, after which a hold time of 1 h was applied under a compacting pressure of 30 MPa. After sintering, the consolidated billets were allowed to furnace cool in-place before extraction from the die. The entire process was conducted in a vacuum chamber kept below 5 Pa.

The sintered billets were subsequently processed by hot extrusion to obtain the reported microstructures. Immediately before extrusion, each billet was pre-heated in an image furnace (RHL-P610C, Advance Riko) to 1000°C at a heating rate of 120°C.min^{-1} in an argon atmosphere (5 L.min^{-1}). After a hold time of 5 min at 1000°C, the billet was pressed through a heated extrusion die of 10 mm diameter (reduction ratio 17.64) at a speed of 6 mm.s^{-1} using a 2000 kN hydraulic press (SHP-200–450, Shibayama Kikai). After processing, the extruded rods were allowed to air-cool to ambient temperatures. The full thermal history of the fabrication process is shown in Fig. 1e, relative to β transus temperatures calculated using the PanTi2023 database of the Pandat Software (Fig. 1f) [23].

2.2. Microstructural and mechanical characterization

Final microstructures were characterised by scanning electron microscopy (SEM, JSM-7100F, JEOL). For analyses, samples were metallographically prepared by standard procedures up to a final vibratory polish in a colloidal silica suspension. Elemental distributions were analysed by backscattered-electron (BSE) imaging, and energy dispersive X-ray spectroscopy (EDS, JED-2300, JEOL), while grain characteristics and phase distributions were investigated by electron backscatter diffraction (EBSD, Hikari, EDAX) with the aid of the EDAX OIM Analysis software. Phase constitution and crystallographic parameters were further investigated by X-ray diffraction (XRD, XRD6100, Shimadzu) using Cu-Kα radiation ($\lambda = 0.154$ nm). Analysis of XRD data was performed with assistance of the BGMN/Profex software [24]. Indexation of XRD peaks was performed with reference data from the Crystallography Open Database (COD) [25,26].

Mechanical performance was evaluated by uniaxial tension testing (Autograph AG-X, Shimadzu), and Vickers micro-indentation hardness testing (HMV-2T, Shimadzu). Miniaturised plate-type tensile test specimens were extracted as close as possible to the centreline of each extruded rod by wire electrical discharge machining. Specimens were machined to a reduced section of 10 mm length, and a cross-section of 2 × 1 mm. Testing was conducted with an initial strain rate of 5×10^{-4} s^{-1}, with load applied along the extrusion direction. Strain was determined from measurements recorded by a non-contact digital video extensometer (TRViewX, Shimadzu). In all samples, yield strength was determined by the 0.2 % offset strain method, while toughness modulus was determined by trapezoidal integration of the tensile datapoints up to fracture.

3. Results and discussion

3.1. Powder characteristics and alloying kinetics

In the sintering of pre-mixed powders, slow-diffusing elements (such as the refractory metals in Ti) are reported to remain concentrated or undissolved near their original particle sources, leading to incomplete alloying [17,27,28]. In such cases, lengthy high-temperature homogenization treatments are often necessary to ensure predictable microstructure formation in the prepared alloys. To avoid this complication and facilitate a single-step sintering process (with in-situ homogenization), large angular CP-Ti particles (31 μm, Fig. 1a) were paired with finer granular Mo particles (3 μm, Fig. 1b) to produce highly sinterable powder mixtures by ball milling. After 6 h of rotary ball milling at 90 rpm, the Mo particles were homogeneously dispersed and partially embedded onto the surfaces of the Ti particles, as exemplified by the Ti-10Mo mixture (Fig. 1c). With an order-of-magnitude difference in size, the large angular facets of the HDH CP-Ti particles provided an abundant surface area for the finer Mo particles to adhere to, creating a uniform core-satellite configuration of Ti and Mo. In turn, this regular distribution of Mo in the powder compact assisted homogenization during SPS [29].

Fig. 1d shows the microstructure and elemental distribution of Ti-10Mo after a single SPS cycle of 1 h at 1100°C and 30 MPa. Despite the low diffusivity of Mo in Ti [30], the microstructure is obviously uniform beyond the scale of the starting powders. Backscattered-electron imaging (Fig. 1d-i) reveals a distinct β-Ti matrix with continuous grain-boundary α and evenly dispersed intergranular α precipitates, which are features indicative of homogenized β-annealed Ti microstructures [31]. Meanwhile, Mo segregation is not detected in EDS mapping of the same area (Fig. 1d-ii), affirming favourable sintering and homogenization behaviour from the core-satellite structured powders. A full analysis of elemental distribution is presented in Supplementary Figure S1(a,b), revealing a highly uniform distribution of Mo in the sintered structures, apart from a slight depletion at the grain-boundary α regions of the samples with lower Mo content (and β stability).

Concurrently, XRD analysis confirms a thorough dissolution of Mo particles across all the sintered Ti-Mo alloys (Fig. 2). The distinct BCC-Mo peaks found in the powders (blue diamonds, Fig. 2a) are completely suppressed after sintering (Fig. 2b), suggesting extensive decomposition of elemental Mo. Conversely, peaks corresponding to BCC β-Ti (green squares, Fig. 2b) begin to emerge, which implies increasing stabilization of the β-Ti phase by the dissolved Mo [32]. These β-Ti peaks exhibit a shift towards higher 2θ angles with increasing Mo content, which is consistent with the substitution of Ti by Mo atoms of slightly smaller atomic radius (Ti: 147 pm, Mo: 139 pm) [33].

Recently, Shahedi Asl et. al reported the presence of remaining undissolved Mo in the preparation of SPS Ti-Mo alloys from mixtures of <60 μm Ti, and <20 μm Mo powders at 1200°C [17]. Despite thoroughly searching for evidence of such features, these were not found in the current dataset. In their study, these defects likely arise from their use of larger Mo particles, which are more resistant to dissolution in the SPS process. Nonetheless, this discrepancy reveals the sensitivity of alloying kinetics to particle size characteristics and sintering. Based on the present empirical findings, fine Mo particles of <5 μm, and SPS parameters of 1 h at 1100°C and 30 MPa appear to be adequate for promoting satisfactory homogenization in as-sintered Ti-Mo alloys with up to 10 wt % Mo.

3.2. Crystallography of extruded alloys

The XRD patterns of the extruded Ti-Mo alloys are shown in Fig. 2c. All samples apart from CP-Ti consisted of α-Ti and β-Ti peaks, with no other detectable phases. The characteristics of the β-Ti peaks followed a similar trend to the as-sintered Ti-Mo alloys, i.e. increasing in relative intensity and exhibiting a peak shift towards higher 2θ angles with increasing Mo content. Once again, this behaviour is attributed to increasing β-stabilization and lattice contraction with increasing Mo content. In contrast, the variations in the α peak positions were less apparent. To characterize the solid solution formation behaviour more extensively, and obtain burgers vector lengths for quantitative modelling, full profile LeBail refinements were performed to obtain the average lattice parameters of the α-Ti and β-Ti phases of the extruded Ti-Mo alloys (Fig. 2d).

The fitted lattice parameters of extruded CP-Ti (Fig. 2d-i) were 0.2951 nm and 0.4686 nm in the *a* and *c* directions respectively, in close alignment with the prototype cell for α-Ti (COD #9008554) [25,26]. In Ti-2.5Mo, the *a*-axis contracts to 0.2949 nm, while the *c*-axis expands slightly to 0.4687 nm. This contraction of the *a*-axis is consistent with partial substitution of Ti atoms in the HCP lattice by Mo [10]. Meanwhile, the simultaneous and counter-intuitive expansion of the *c*-axis appears suggest an increase in interstitial solutes. Oxygen and nitrogen are known to preferentially occupy octahedral interstices in the HCP

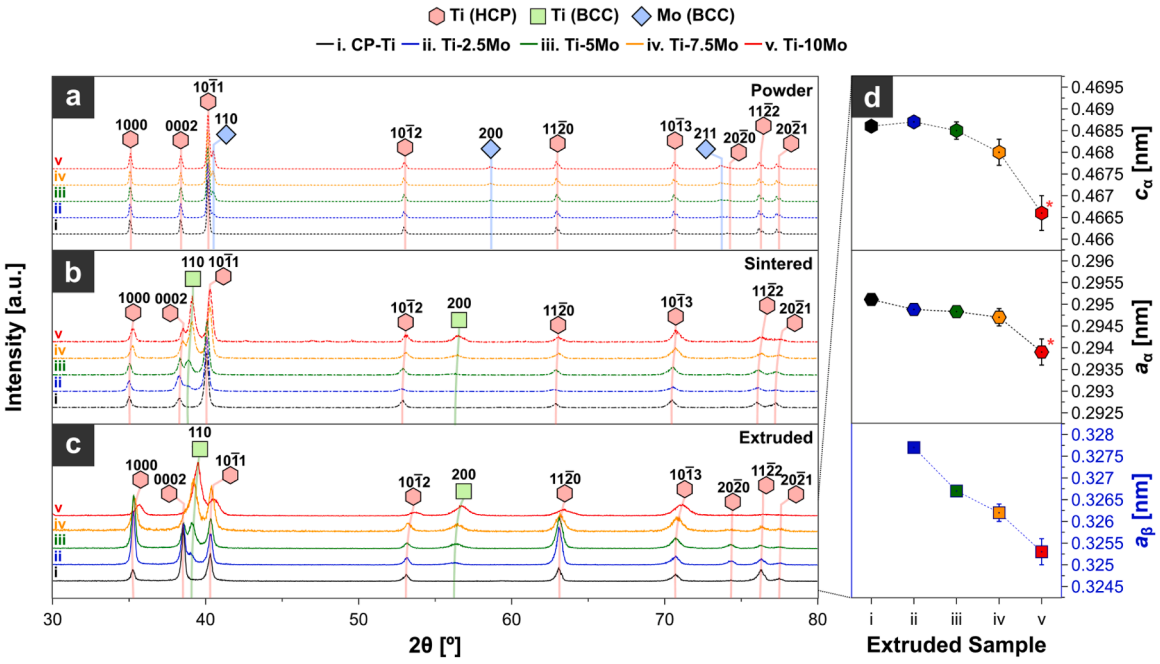

Fig. 2. X-ray diffraction profiles of (i) CP-Ti, (ii) Ti-2.5Mo, (iii) Ti-5Mo, (iv) Ti-7.5Mo, and (v) Ti-10Mo, in (a) milled powders, (b) as-sintered condition, (c) as-extruded condition. (d) Lattice constants of α and β phases in the extruded samples, as refined from the profiles shown in (c). (*) Note the fitted lattice parameters of α-Ti in extruded Ti-10Mo may not be accurate due to poorly defined peaks.

lattice, causing an anisotropic expansion of the *c*-axis [34]. To support this theory, the O, N and H contents were measured by the inert-gas-fusion method to track changes throughout the processing stages (Table 1). While no significant change was observed between processing stages, the evaluated O content in the extruded Ti-Mo alloys was confirmed to be 11 %–26 % (0.03 wt%–0.072 wt%) higher than identically processed CP-Ti. The proportional increase with Mo addition suggests the starting Mo powder is the most likely source of this introduced oxygen. This trend explains the observed *c*-axis expansion in Ti-2.5Mo.

Between Ti-2.5Mo and Ti-7.5Mo, both *a* and *c* axes proceed to linearly contract to 0.2947 nm and 0.468 nm respectively, as the expansion from interstitial O is counteracted by contraction from substitutional Mo. Finally, Ti-10Mo exhibits an abrupt contraction of both *a* and *c* parameters to 0.294 nm and 0.466 nm respectively. These abnormally low parameters in Ti-10Mo may potentially arise from the distortion of α-Ti peaks by a small fraction of α'' domains. Orthorhombic α'' is a metastable phase reported in water quenched Ti-Mo alloys, with a geometric arrangement somewhere between the β and α lattice structures [35]. However, this theory is impossible to confirm as the α-Ti peaks are substantially broadened with peak centres convoluted within the stronger β-Ti peaks of this sample; the distinct split peaks of α'' are also not observed. Meanwhile, a more reliable analysis of the β-Ti peaks reveals a linear contraction of the *a*-axis from 0.3277 nm to 0.3253 nm between 2.5 wt% and 10 wt% of Mo addition. Fitting a linear trendline to the refined β-Ti lattice parameters suggests a contraction of 0.308 pm per wt% Mo or 0.592 pm per at% Mo, with an intercept of 0.3284 nm, and an R^2 coefficient of 0.986. This trend is in good agreement with prior reports [10].

Table 1
Oxygen, nitrogen and hydrogen contents across various stages of processing.

Stage	Material	Content [wt%]		
		O	N	H
Milled Powder	CP-Ti	0.298	0.033	0.029
	Ti−2.5Mo	0.316	0.018	0.028
	Ti−5Mo	0.331	0.019	0.029
	Ti−7.5Mo	0.349	0.019	0.029
	Ti−10Mo	0.349	0.022	0.033
Sintered	CP-Ti	0.288	0.023	0.034
	Ti−2.5Mo	0.288	0.020	0.030
	Ti−5Mo	0.300	0.018	0.031
	Ti−7.5Mo	0.311	0.019	0.031
	Ti−10Mo	0.328	0.021	0.026
Extruded	CP-Ti	0.281	0.021	0.035
	Ti−2.5Mo	0.313	0.020	0.033
	Ti−5Mo	0.330	0.017	0.035
	Ti−7.5Mo	0.337	0.018	0.034
	Ti−10Mo	0.353	0.021	0.031

3.3. Microstructural characteristics and formation mechanisms

The morphologies of these phases are revealed by EBSD analysis (Fig. 3). In this panel of images, the microstructures of each composition are shown in backscattered electron images (Fig. 3a), grain boundary maps (Fig. 3b), and orientation maps of the α-Ti (Fig. 3c) and β-Ti phases (Fig. 3d), taken from the same area. The orientation maps are colour coded by inverse-pole-figure (IPF) along the extrusion direction to reveal the influence of processing. In complete alignment with the XRD trends, increasing Mo content is clearly seen to promote the β phase at the expense of the α phase. Across the various compositions, the phase fractions transition from near-full-α (98.8 area% in Ti-2.5Mo), to near-full-β (97.0 area% in Ti-10Mo). Based on successfully indexed EBSD points with a confidence index metric (CI) of greater than 0.1, Ti-7.5Mo appears to be the critical composition at which microstructures become predominantly β, with 50.4 area% β, and 49.7 area% α. Spatially, this change in phase fraction is observed as a refinement of α colonies (average 62.5 μm in CP-Ti) towards ultra-fine lath precipitates (< 1 μm) contained within larger retained β grains (average 34 μm in Ti-10Mo). Full statistical distributions for each phase are presented in Supplementary Figure S2**.** The morphology of these finer α-Ti precipitates in Ti-7.5Mo and Ti-10Mo are difficult to resolve by EBSD, and are separately presented in Fig. 4a-b.

All microstructures exhibit clear evidence of deformation processing, with a distortion of β/prior-β grains towards the extrusion direction

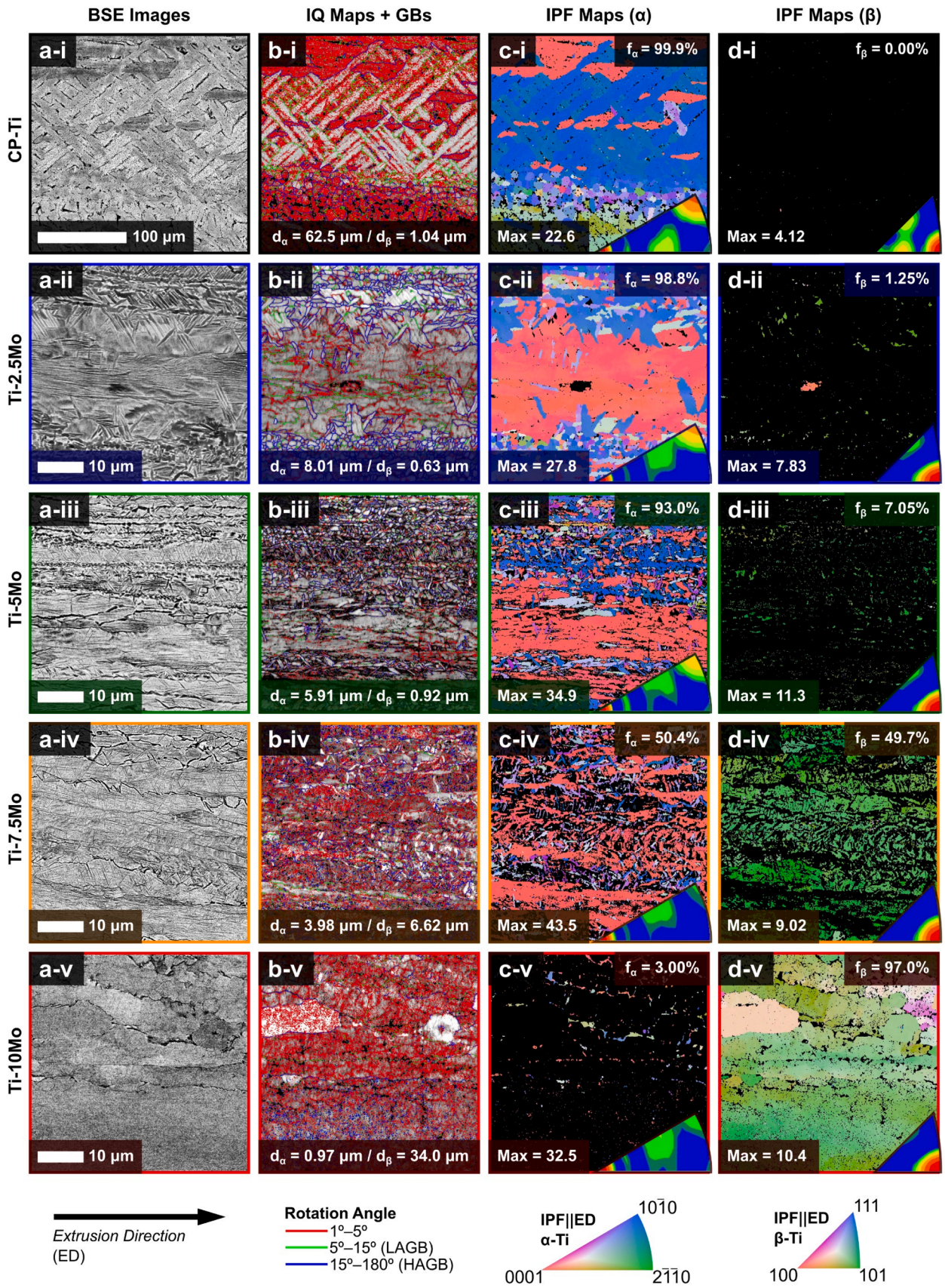

Fig. 3. Microstructures of (-i) CP-Ti, (-ii) Ti-2.5Mo, (-iii) Ti-5Mo, (-iv) Ti-7.5Mo and (-v) Ti-10Mo as observed in (a) backscattered electron images, (b) composited image quality and grain boundary maps, and orientation maps of the (c) α and (d) β phases, coloured with respect to the extrusion direction.

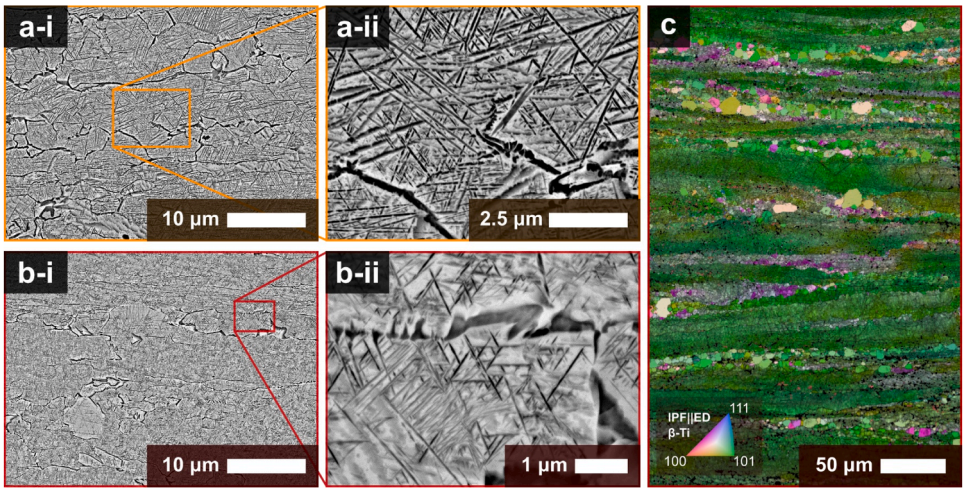

Fig. 4. High-magnification backscattered electron images of fine secondary α laths present in (a) Ti-7.5Mo and (b) Ti-10Mo. (c) Low-magnification composite map of image quality and β phase orientation in Ti-10Mo, revealing recrystallized necklace structures.

(ED). These elongated grains are clearly delineated by distinct grain-boundary α (GB-α) in Ti-5Mo, Ti-7.5Mo and Ti-10Mo (Fig. 3a(iii-v)). In the latter samples, where the deformed β structure is mostly preserved, these grains are found to contain a high density of local disorientations of less than 5° (mapped in red in Fig. 3b). Such a large concentration of low-angle disorientations suggests a substantial amount of dislocations and sub-grains, which form upon plastic deformation to accommodate the imposed lattice strains [36]. Concurrently, these β grains also exhibit a strong alignment of $<110>_{\beta}$ along ED (mapped as green in Fig. 3d), with a texture intensity of around 10 multiples of uniform density (MUD). In β-Ti alloys deformed above T_{β}, such strong textures are reported to arise from the re-orientation and alignment of $\{110\}_{\beta}$ slip systems along the directions of load and strain (i.e. the radial and axial directions of the extrusion die) [37]. Additionally, a weaker $<112>_{\beta}||$ED texture of 1–1.5 MUD near is also detected in some samples. These latter orientations appear to arise from a small fraction of dynamically re-crystallized β grains, which produces characteristic necklace formations of fine equiaxed grains (5–10 μm) along some grain boundaries in Ti-10Mo (Fig. 4c). This mechanism is reported in other Ti alloys deformed at higher super-transus temperatures (in the present work, 150–230°C above T_{β}), and are thought to result from inhomogeneous deformation with intensified strains at grain boundaries [38].

Across all samples, the α grains are configured in micro-textured bands with $<0001>_{\alpha}||$ED and $<10\text{–}10>_{\alpha}||$ED orientations (coloured red and blue respectively in Fig. 3c). For discussion purposes, these $<0001>_{\alpha}||$ED areas are henceforth referred to as basal textured regions, while the $<10\text{–}10>_{\alpha}||$ED areas are henceforth referred to as prismatic textured regions. Both basal and prismatic textures are clearly related to the strong $<110>_{\beta}||$ED texture of the extruded β phase via the Burgers orientation relationship (BOR, $\{110\}_{\beta}||\{0001\}_{\alpha}$, $<1\text{–}11>_{\beta}||<11\text{–}20>_{\alpha}$) [39]. Considering the slip systems of α-Ti, this produces an interesting mixture of grains oriented with favourable prismatic $<a>$ slip (prismatic textured), and effectively impossible $<c>$ slip (basal textured) [40]. In the latter fraction of grains, the Schmid factors of the prismatic $<a>$ slip systems are close to zero, and deformation can only realistically proceed by $<c+a>$ slip, grain rotation, or grain boundary sliding mechanisms [41].

Aside from texture, the two regions are also morphologically distinct; where each basal textured region is formed by a single colony of α lamellae, oriented at 0° to ED; while each prismatic textured region consists of multiple finer colonies formed by equiaxed grains and laths oriented at 45° to ED. The colony boundaries are demarked as the blue high-angle grain boundaries (HAGBs) in Fig. 3b, revealing a bimodal distribution of effective α grain sizes.[1] Both basal and prismatic textured α regions are incrementally suppressed and refined with increasing Mo concentration. This effect naturally arises from the depression of the β transus temperature with increasing Mo concentration, which suppresses the recrystallization and growth of α after the extrusion process. Calculated phase diagrams suggest β transus temperatures (T_{β}) of 852°C, 825°C, 797°C and 773°C for Ti-2.5Mo, Ti-5Mo, Ti-7.5Mo and Ti-10Mo, respectively (Fig. 1g) [23]. Assuming similar air-cooling rates across the various compositions, the depression of the β transus delays the onset of the diffusive β → α transformation, while its conclusion is accelerated by the elevated thermodynamic stability of the β phase; thereby narrowing the time and temperature window for α formation.

This β-stability mediated microstructural evolution from Ti-10Mo to Ti-2.5Mo provides useful insights into the formation mechanisms of the α structures, as each increment effectively represents a snapshot in the β → α transformation. In the early stages of the transformation (captured in Ti-10Mo), GB-α heterogeneously nucleates between the β grains, while finer α laths of <0.1 μm thickness are found throughout the β grain interiors (Fig. 4b-i). At higher magnification (Fig. 4b-ii), these laths appear to originate from branching serrations in the GB-α, suggesting they form by a Widmanstätten-type mechanism rather than a martensitic transformation. Both GB-α and Widmanstätten-α are known to follow the BOR [42,43], thereby accounting for the strong basal and prismatic textures (see IPF in Fig. 3c-v). This mechanism also accounts for the morphological orientations of the α laths at 0° and 45° to ED, as these lath orientations are related to the habit planes of different α variants [42].

Meanwhile, in Ti-7.5Mo, the reduced β-stability and improved atomic mobility enables the growth of these α features into continuous GB-α and coarsened laths (Fig. 4a). This coarsening allows these laths to be partially resolved by EBSD (Fig. 3c-iv), revealing strong basal texture in the α laths oriented at 0° to ED, and strong prismatic texture in the α laths oriented at 45° to ED. This correlation between morphological and crystallographic orientations affirms their origin from BOR habit planes. These features progressively coarsen with at the lower Mo concentrations and are also observed in the CP-Ti sample (suggesting they originate from processing rather than composition). Across all α and α+β compositions (CP-Ti to Ti-7.5Mo), the basal textured colonies appear to always coarsen more substantially than the prismatic colonies, producing a heterogeneous grain size distribution. This discrepancy likely

[1] Effective grain size referring to collections of grains with identical crystallographic orientation and slip characteristics.

arises from the favourable orientation of the basal textured laths along the elongated prior-β structure, allowing uninterrupted longitudinal growth of the laths along ED. Meanwhile, the prismatic laths must compete with neighbours with more variants (with <c> axes distributed randomly along the radius of the extrusion), leading to more refined colony structures. An investigation of elemental distribution (Supplementary Figure S1(c,d)) confirms no correlation between Mo concentration and the size and texture characteristics, suggesting the bimodality predominantly arises from the variant selection and growth inhibition processes.

Additionally, a small fraction of equiaxed α grains are observed to be interlaced amongst the finer colonies of the prismatic textured regions. These grains tend to show prismatic, or <11–20>||ED textures and are consistent with spheroidized α lamellae. Such grains are reported to form both dynamically (during deformation in the α+β region), and statically (usually by post-annealing) [20]. Considering these become more prominent with reduced Mo content and make up a considerable fraction of the CP-Ti extrusion (bottom half of Fig. 3c-i), it is more probable that temperatures are dropping below T_β during the extrusion of these composition. However, a contribution from self-annealing during the air-cooling process cannot be completely excluded.

3.4. Mechanical properties

The room-temperature engineering stress-strain curves of the extruded Ti-Mo alloys are presented in Fig. 5a, showing a large range of tensile properties across the five compositions. The trends in tensile properties, with respect to Mo content are presented in Fig. 5b, and numerically summarized in Table 2. Both yield (σ_{YS}) and ultimate tensile strengths (σ_{UTS}) exhibit a monotonic rise from ~500 MPa to ~1500 MPa from 0–10 wt% Mo, while ductility (measured by total elongation to failure, ε_F) appears to remain quite stable up to 5 wt% Mo. At 7.5 wt% of Mo addition and beyond, ε_F abruptly drops. However, these latter materials are remarkably strong with Ti-10Mo exhibiting exceptional strengths of $\sigma_{YS} \approx 1380$ MPa / $\sigma_{UTS} \approx 1500$ MPa, and an acceptable total elongation of $\varepsilon_F \approx 10$ %. Meanwhile, Ti-2.5Mo and Ti-5Mo demonstrate exceptional tensile toughness (U_T). U_T is a metric used to quantify the capacity of energy absorbed by a material before fracture (typically defined by the total area under the tensile curve or approximated by multiplying σ_{UTS} by ε_F). In these samples, the remarkable increase in

Table 2
Tensile and microindentation hardness properties of as-extruded materials.

Material	Tensile Properties				Hardness	
	σ_{YS} [MPa]	σ_{UTS} [MPa]	ε_F [%]	U_T [MJ. m^{-3}]	ND [$HV_{0.1}$]	ED [$HV_{0.1}$]
CP-Ti	476.8 ± 1	626.4 ± 3	33.9 ± 3	199.5 ± 19	234.0 ± 17	225.3 ± 17
Ti−2.5Mo	821.5 ± 7	933.6 ± 1	31.9 ± 1	287.4 ± 10	301.5 ± 17	290.3 ± 15
Ti−5Mo	1007.9 ± 19	1112.9 ± 16	34.1 ± 6	361.3 ± 73	343.6 ± 11	322.0 ± 12
Ti−7.5Mo	1226.5 ± 4	1317.3 ± 4	13.6 ± 0	166.4 ± 5	385.9 ± 10	393.8 ± 7
Ti−10Mo	1382.8 ± 9	1496.5 ± 23	9.9 ± 1	132.5 ± 19	431.7 ± 13	437.2 ± 9

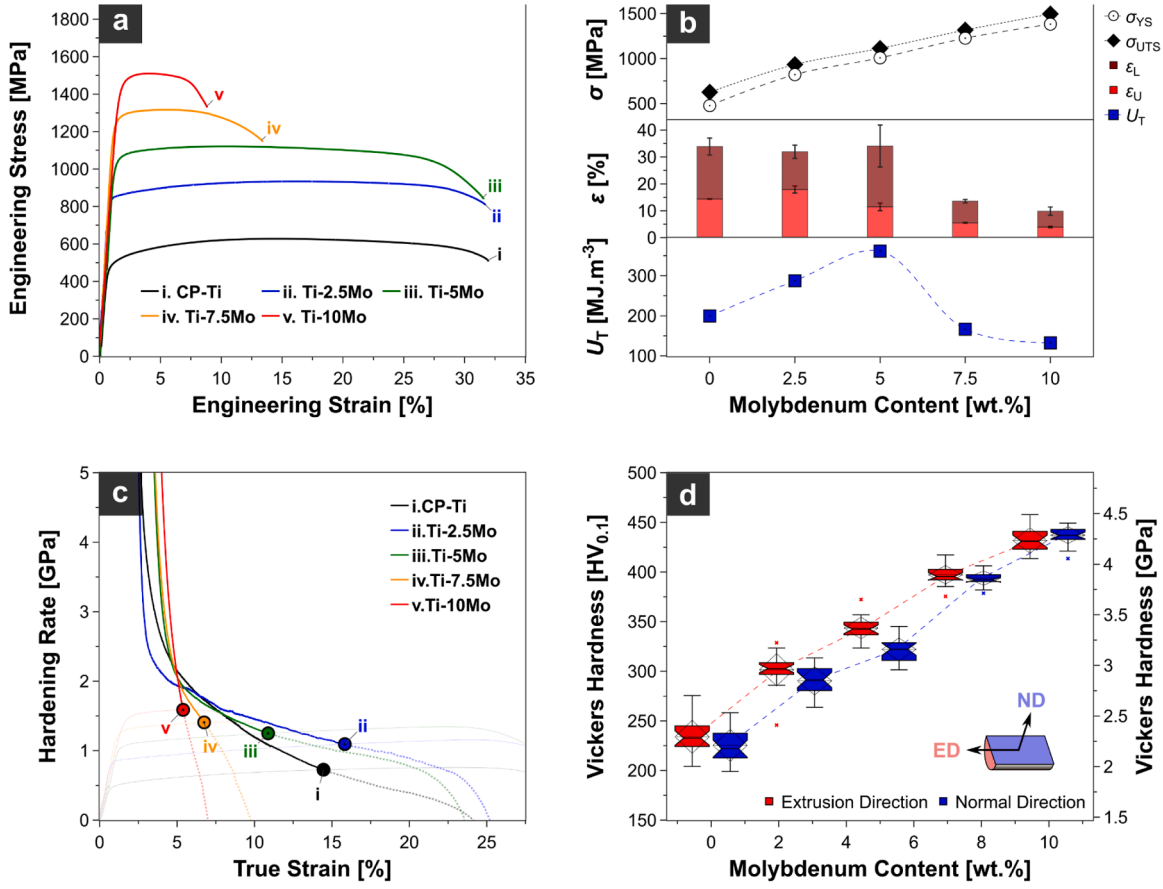

Fig. 5. (a) Room-temperature tensile curves of as-extruded (i) CP-Ti, (ii) Ti-2.5Mo, (iii) Ti-5Mo, (iv) Ti-7.5Mo, and (v) Ti-10Mo samples. (b) Trends of yield strength (σ_{YS}), ultimate tensile strength (σ_{UTS}), local elongation (ε_L), uniform elongation (ε_U), and tensile toughness (U_T) in extrusions of varying Mo content. (c) Hardening curves of the same samples, with necking points identified by Considères construction. (d) Vickers micro-identation hardnesses of the same samples, on planes perpendicular to the extrusion (ED) and normal directions (ND).

strength with limited sacrifice to total elongation significantly enhances the tensile toughness of these samples, producing an exceptional 180 % increase in U_T from 199 MJ.m^{-3} in CP-Ti to 361 MJ.m^{-3} in Ti-5Mo.

Strain hardening curves are presented in Fig. 5c to analyse the uniform elongation (ε_U) and hardenability trends. From the necking instability points (round markers, identified by the Considère's construction method [44]), ε_U is first seen to increase slightly from a true strain of 14.5 % (CP-Ti) to 15.8 % (Ti-2.5Mo) before the trend reverses with further Mo addition (to 10.9 %, 6.6 % and 5.9 % for Ti-5Mo, Ti-7.5Mo and Ti-10Mo, respectively). This pattern is also observed in the hardenability, which also initially increases at 2.5 wt% Mo, before diminishing below the CP-Ti baseline with further addition. These reductions in uniform elongation and hardenability are likely associated with the higher dislocation densities in the high Mo samples after extrusion (as indicated by the high disorientations in the retained β samples shown Fig. 3b). Conversely, the relatively crystalline α laths retain good hardenability characteristics and suppressing the onset of necking.

Like strength, micro-indentation hardness (Fig. 5d) also presents a monotonic increase from an average of 230 $HV_{0.1}$ in CP-Ti to an average of 434 $HV_{0.1}$ in Ti-10Mo. Notably, in CP-Ti, Ti-2.5Mo and Ti-5Mo, the planes perpendicular to the extrusion direction were slightly harder than the planes perpendicular to the normal direction; while the Ti-7.5Mo and Ti-10Mo samples showed more comparable hardnesses across the two planes. The increased anisotropy at lower Mo content likely reflects the bi-modal α texture of these samples. Indentations performed in the extrusion axis are simultaneously hardened by both the <*c*> axis orientation of the basal textured regions, and the refined grain structure of the prismatic textured regions; while the indentations performed in the normal direction encounter the more deformable <*a*> directions of the coarse basal textured regions [40]. Meanwhile, the BCC symmetry of β expose favourable {110} slip systems to both directions, which produces relatively isotropic performance in the β dominant samples.

Considering the exceptional properties of Ti-2.5Mo, and Ti-5Mo, the deformed microstructures were further investigated to provide insight into the deformation distribution in these materials. Fig. 6 presents kernel-average-misorientation (KAM) maps of the materials before and after tensile testing (the deformed structures are taken from the uniformly deformed section). Under deformation, KAM values are expected increase in regions of high-strain due to increased lattice curvature from increased dislocation activity, thereby revealing the partition of strain in a material. As seen in a cross-comparison of the IPF and KAM maps in Fig. 6(a-b), both basal (red) and prismatic textured (blue) regions show similar KAM intensity in the undeformed structures. However, KAM values intensify much more substantially in the prismatic textured regions after deformation (Fig. 6(c-d)). Meanwhile, the KAM value in the centres of individual basal textured grains (marked by white arrows in Fig. 6(c-d)) remain very low (<1.5°), which suggests limited deformation in these areas.

Additionally, the morphology and crystallographic orientation of these basal textured grains do not appear to change substantially, remaining as coarse lamellar colonies with major axes, and <*c*> directions oriented along ED. Twinning is also not observed. Considering the KAM values in these areas only increase near their boundaries, the only reasonable deformation mechanisms in these grains appear to be the intrinsically hard <*c*+*a*> slip [40], or more complex grain boundary sliding mechanisms [41]. On the other hand, the prismatic textured laths can be seen to rotate towards ED in support of plasticity. The undeformed prismatic grains typically exhibit major axes with 45° angle to ED, while the deformed prismatic grains exhibit angles of <30° to ED. Considering the crystallographic texture of these regions also remain unchanged, this morphological rotation is most likely supported by progressive slip rather than bulk crystal rotation. Overall, this periodic, elongated arrangement of these soft and hard regions causes the microstructure to behave like a fibre composite under tensile loading, enabling simultaneous strength and ductility. The basal textured regions provide strength, while the prismatic textured regions support plasticity.

Fig. 7 shows the post-fracture surfaces of the tensile test specimens. In line with the observed tensile properties, fracture features transition

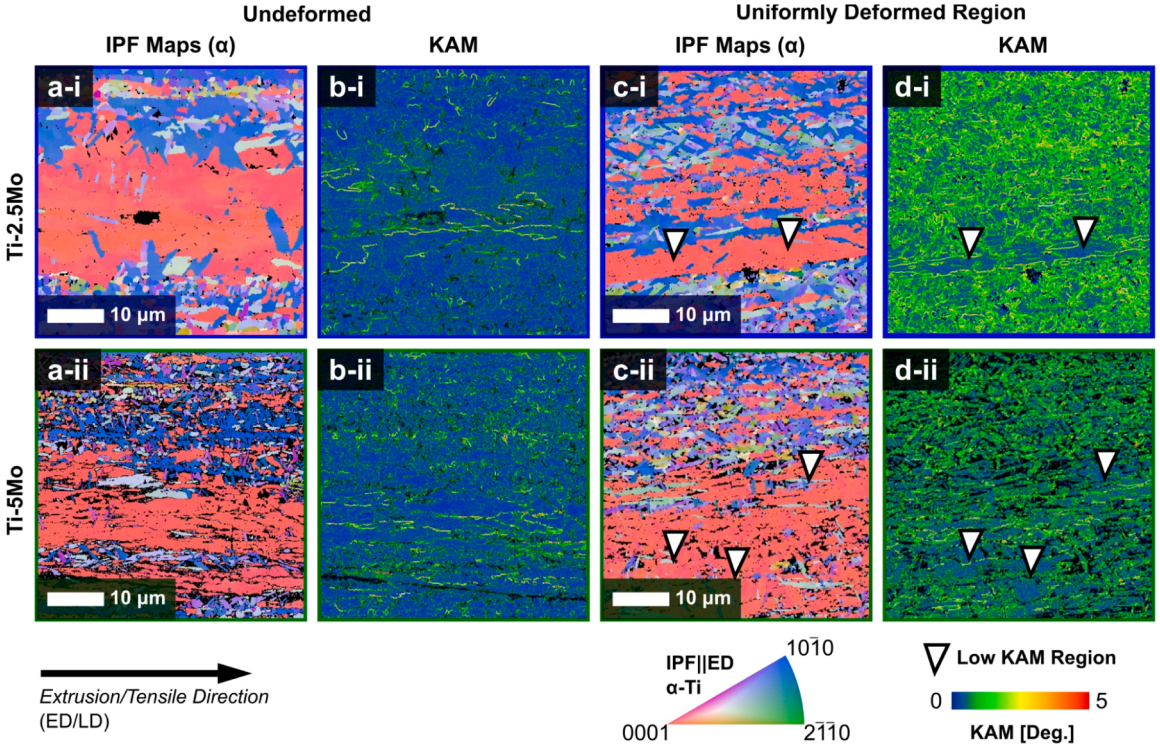

Fig. 6. Microstructures of (a,b) undeformed and (c,d) deformed microstructures of (-i) Ti-2.5Mo, and (-ii) Ti-5Mo, as shown in (a,c) orientation maps of the α phase and (b,d) kernel-average-misorientation maps. The deformed microstructures are captured from the uniformly deformed region of the tensile specimen (i.e., outside of the necked region).

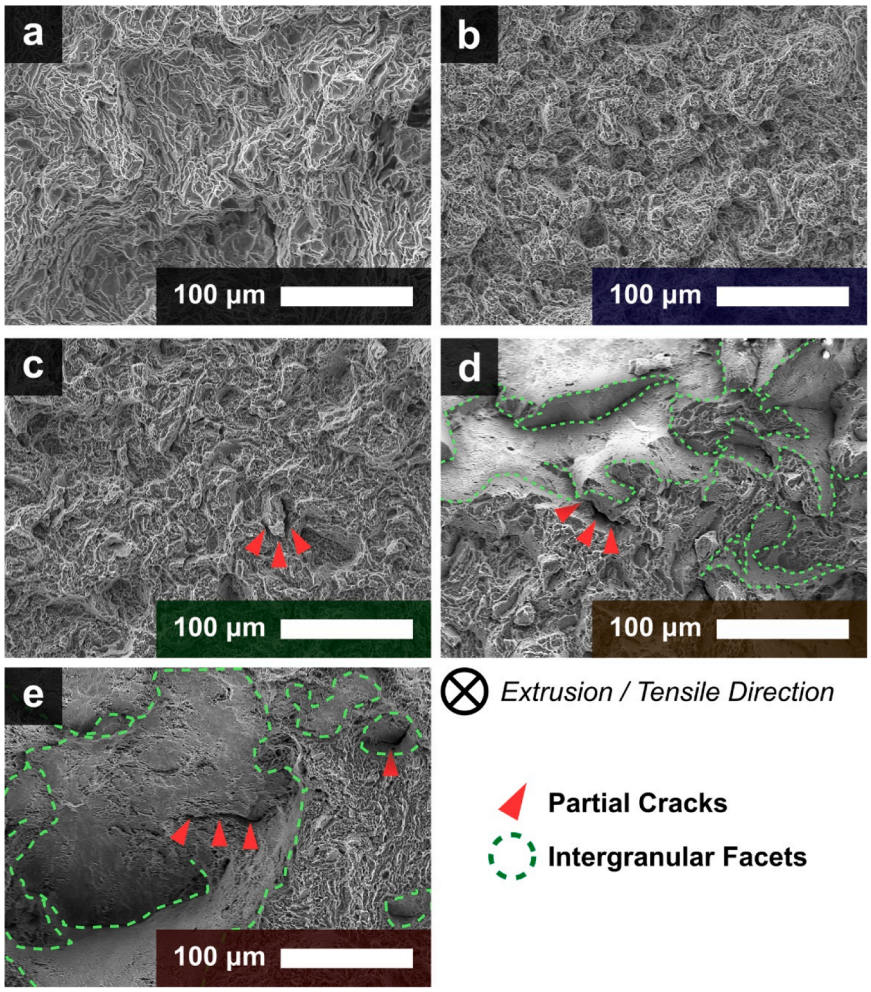

Fig. 7. Fracture surfaces of as-extruded (a) CP-Ti, (b) Ti-2.5Mo, (c) Ti-5Mo, (d) Ti-7.5Mo and (e) Ti-10Mo showing a transition from fine ductile dimples to a multi-modal fracture with both dimpled regions and larger intergranular fracture facets.

from finely dimpled surfaces (ductile nucleation and coalescence of voids) in 0–5 wt% Mo (Fig. 6a-c), to a mix of dimples and larger facets (semi-brittle fracture) in 7.5 and 10 wt% Mo (Fig. 6d-e). Compared to CP-Ti, the dimple features in Ti-2.5Mo and Ti-5Mo are more refined, correlating with the refinement of grain structures [45]. Some partial cracks are also observed in Ti-5Mo, likely arising from the small fraction of retained β in this composition. As previously discussed, these retained β grains are substantially strain hardened and likely to serve as crack nucleation sites. However, the cracks formed in Ti-5Mo appear to be prevented from propagating substantially by the surrounding grain structure, as they must either cleave through the continuous basal textured colonies or propagate through the complex boundaries of the finer prismatic colonies. With increasing β fraction in Ti-7.5Mo and Ti-10Mo, semi-brittle failure occurs with a mix of ductile fracture and intergranular fracture at β/GB-α/β interfaces. These samples appear to retain acceptable (i.e. >10 % ε_F) ductility due to relative discontinuity of GB-α sections with orientations perpendicular to the tensile (and extrusion) direction.

3.5. Strengthening mechanisms

In consideration of to the microstructures in Fig. 3, the large range of mechanical properties can clearly be attributed to the large variation in phase constitution and grain morphology between samples of varying Mo content. To clarify the strengthening mechanisms responsible for these exceptional properties, a quantitative analysis was prepared from theoretical models and experimentally obtained parameters. Specifically, theoretical models for room-temperature conditions and quasi-static strain rates were selected. For each phase, the intrinsic lattice strength (σ_{PN}) was considered in combination with contributions from solid-solution strengthening ($\Delta\sigma_{SS}$), dislocation strengthening ($\Delta\sigma_{DS}$), and grain-boundary strengthening ($\Delta\sigma_{GB}$) (Eq. 1). This produced an estimated yield strength for the phase ($\sigma_{YS,i}$), which was subsequently weighted by the area fraction of the phase (f_i) from EBSD analysis (Eq. 2).

$$\sigma_{YS,est} = \sigma_{PN,i} + \Delta\sigma_{SS,i} + \Delta\sigma_{DS,i} + \Delta\sigma_{GB,i} \quad (1)$$

$$\sigma_{YS} = f_\alpha\sigma_{YS,\alpha} + f_\beta\sigma_{YS,\beta} \quad (2)$$

The intrinsic lattice strength is related to the resistance to dislocation propagation by the Peierls-Nabarro (PN) stress. This is approximated by the critically resolved shear stress (τ_{CRSS}) of a high-purity lattice, free of other strengthening mechanisms. In high purity α-Ti, experimental studies into high purity titanium have reported minimum τ_{CRSS} values of ~90 MPa for the prismatic slip system [40]. However, the intrinsic lattice friction of high-purity β-Ti is impossible to determine considering its instability at room temperatures. Nonetheless, BCC crystals are well reported to exhibit higher P-N stresses than their HCP counterparts and are reported to exhibit P-N stresses in the range of 5×10^{-3} times the shear modulus [46,47]. On the basis of this relationship, an estimated τ_{CRSS} value of 195 MPa was adapted for β-Ti based on a shear modulus of 39 GPa [48]. From these values, $\sigma_{PN,i}$ was calculated using

experimentally obtained Taylor factors for each phase (M_i) in every composition (Eq. 3).

$$\sigma_{PN,i} = M_i \tau_{CRSS,i} \tag{3}$$

Meanwhile, the solid-solution strengthening effects in each phase were modelled using a Labusch-type multi-component solid solution strengthening model [49]. This model accounts for the combined hardening effect of multiple solutes by their individual atomic concentrations (c_j), and hardening parameters (B_j) in each solvent phase (Eq. 4). The values of $B_{j,i}$ are a function of shear modulus and lattice parameter mismatches between solutes atoms and the solvent lattice, which generates additional resistance against dislocation activity. For Ti, the parameters for O, N and Mo in both α and β phases are well reported in literature [48,50,51]. These values have been adapted for the present work. To account for the atypical textures of the extruded materials, the hardening parameters from literature are re-adjusted for the experimentally observed Taylor factors ($M_{expt.}$) based on the Taylor ($M_{lit.}$) or Schmid ($m_{lit.}$) factors of the relevant work as per Eq. 5[2].

$$\Delta\sigma_{SS,i} = \left(\sum_j B_{j,i}^{\frac{3}{2}} c_{j,i}\right)^{\frac{2}{3}} \tag{4}$$

$$B_{adj.} = B_{lit.}\frac{M_{expt.}}{M_{lit.}} = B_{lit.} M_{expt.} m_{lit.} \tag{5}$$

Continuing with lattice level effects, the dislocation strengthening component was predicted by the Taylor relationship (Eq. 6), where the increase in σ_{YS} from the entanglement of dislocations is modelled as a function of the Taylor factor, the shear modulus (G), the Burgers vector (b), a constant (α) and the density of dislocations (ρ). For each phase, M and ρ were calculated from EBSD data, while values for G_α and G_β were taken as 45.6 and 39 GPa, respectively [48]. Meanwhile, a value of 0.2 was adapted for both α_α and α_β based on reports of similarly deformed Ti alloys [52].

$$\Delta\sigma_{DS,i} = M_i G_i b_i \alpha_i \sqrt{\rho_i} \tag{6}$$

Finally, the grain-boundary strengthening component was predicted by the well-established Hall-Petch relationship (Eq. 7), where the increase in σ_{YS} from the resistance of dislocation transfer across grain boundaries is modelled by the grain size d and a material dependant constant k. Average equivalent grain diameters were taken from reconstructed EBSD grains, while values of 0.2 MPa.m^{-2} for k_α, and 0.75 MPa.m^{-2} for k_β were adapted from literature [27,48]. A more complex consideration of low-angle grain boundary (LAGB) and HAGB influences was not considered as there was no significant variation in LAGB/HAGB ratio between α dominant samples (Supplementary Table S1). Meanwhile, such an analysis cannot sufficiently account for the phase differences in the α+β samples.

$$\Delta\sigma_{GB,i} = k_i d_i^{-\frac{1}{2}} \tag{7}$$

The values predicted for σ_{YS} using this model are compared with experimental values in Fig. 8a, while the experimental parameters and variables are numerically outlined in Table 3. Here, the total solid solution strengthening contribution is presented, however a detailed breakdown of the individual solute contributions in each phase is available in Supplementary Table S2. Overall, a reasonable fit is obtained by inputting experimental derived parameters into the solid-solution strengthening, dislocation strengthening and grain refinement models. Evidently, oxygen solid-solution-strengthening plays an important role in producing the baseline strength observed in pure Ti alloys (~400 MPa), however the remarkable strengthening observed with Mo addition is predominantly from grain refinement and dislocation hardening components. These are both effects significant effects produced by the thermomechanical processing of the β-stabilized compositions.

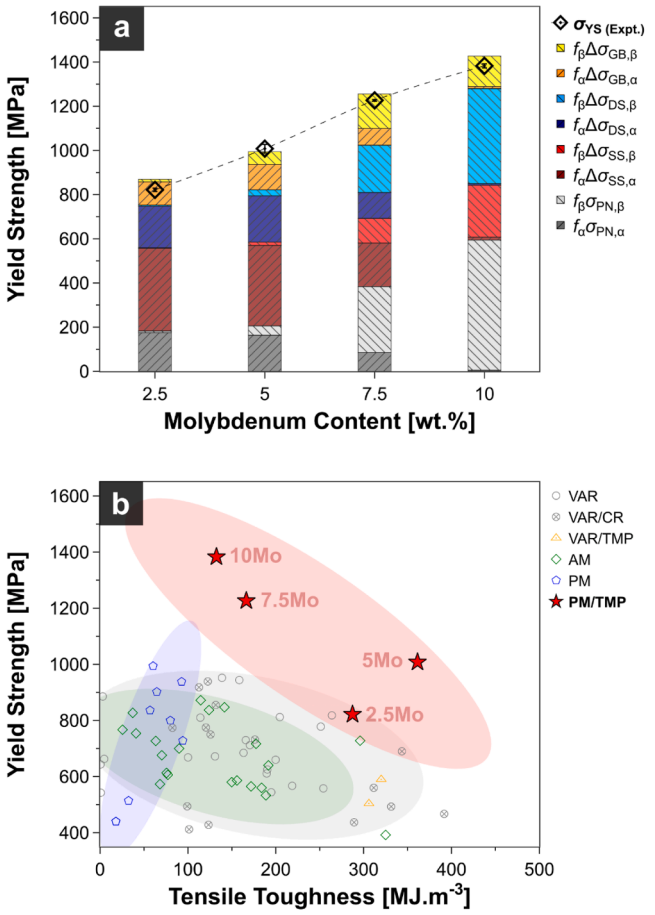

Fig. 8. (a) Theoretically modelled strengthening contributions from intrinsic strength (σ_{PN}), solid solution strengthening (σ_{SS}), dislocation strengthening (σ_{DS}), and grain boundary strengthening (σ_{GR}) weighted by phase fractions (f_α and f_β). (b) Yield strengths and tensile toughnesses in the present binary Ti-Mo alloys compared to reported properties in literature by various vacuum-arc-remelting (VAR) [56–58], additive manufacturing (AM) [59–63], and powder metallurgy (PM) based methods [16,17]. Reports from cold-rolled (CR) [64–66] and thermomechanically processed (TMP) [18,19] samples are separately marked.

Other studies into metastable β-Ti alloys have reported possible influences on mechanical behaviour from orthorhombic α'' and hexagonal ω precipitates [53]. Specifically, martensitic α'' is usually associated with transformation and twinning induced plasticity (TRIP/TWIP), while ω precipitates are reported to follow a strength-ductility trade-off consistent with age hardening [54]. However, the characterization methods used in the present study are inadequate for a reliable detection and analysis of these phases due to their small crystallite sizes and similar interplanar spacings. In XRD, these phases are usually reported as broad, low-intensity peaks, and are often convoluted into nearby α/β peaks due to their similar interplanar spacings. For the same reasons, Hough-based EBSD struggles to differentiate the phases and cannot provide enough spatial resolution to resolve fine nano-domains [55]. However, considering TRIP/TWIP characteristics are not observed in the tensile behaviour of the present materials, and the cooling conditions do not favour a large fraction of these phases, a deeper characterization of these metastable phases will entail further work beyond the scope of the

[2] Some reporting works empirically fit hardening parameters to their experimentally obtained Schmid factors for the prismatic slip system. These are approximated into Taylor factors by assuming a reciprocal relationship, i.e. $M = 1/m$

Table 3
Experimentally derived parameters used for theoretical modelling of strengthening mechanisms and estimated strengthening contributions.

Material	Experimental Parameters							Theoretical Estimates				
	f_β [area%]	M_α [-]	M_β [-]	ρ_α [10^{15} m^{-2}]	ρ_β [10^{15} m^{-2}]	d_α [μm]	d_β [μm]	σ_0 [MPa]	$\Delta\sigma_{SS}$ [MPa]	$\Delta\sigma_{DS}$ [MPa]	$\Delta\sigma_{GB}$ [MPa]	$\sigma_{YS,est}$ [MPa]
Ti−2.5Mo	1.30 %	1.97	2.98	1.29	3.61	8.01	0.63	182.6	376.7	193.4	116.8	869.5
Ti−5Mo	7.10 %	1.95	3.11	1.83	3.22	5.91	0.92	205.8	379.3	236.8	172.8	994.7
Ti−7.5Mo	49.70 %	1.89	3.1	2.08	3.99	3.98	6.62	383.7	309.0	331.4	231.6	1255.7
Ti−10Mo	97.00 %	1.96	3.07	1.99	4.30	0.98	34.0	594.3	248.0	437.7	147.0	1427.0

study.

In the current strengthening model, any effect from the presence of these precipitates is likely to be accounted for by the dislocation strengthening component, which relies on the disorientations captured in EBSD. Lattice distortions produced by nanoscale ω precipitates, or fine α'' martensite would effectively be captured and modelled as additional dislocations in the β-phase. Therefore, any strengthening produced by the limited presence of these elements would be effectively treated as dislocations in the β lattice. Nonetheless, given the remarkable strength-ductility balance achieved in this series of alloys, the nature of these precipitates are certainly an interesting topic of study for future work, alongside further investigation of dynamic mechanical properties like fatigue. In the meantime, the excellent performance from the current series of Ti-Mo is self-evident in a comparison of σ_{YS} and U_T from a broad survey of other reported Ti-Mo alloys prepared by other methods (Fig. 8b). These datapoints include various binary compositions of 1.5 wt%–20 wt% Mo prepared by vacuum arc remelting (VAR), various additive manufacturing techniques (AM), and other powder metallurgy methods (PM). Although extrusions are limited in applicability, the strength-ductility balance achieved in the present work vastly outperforms all of these prior works. This finding clearly highlights a strong potential for Ti-Mo alloys prepared by other thermomechanical processing routes, which appears to be underrepresented in the literature.

4. Conclusions

In this work, a series of binary Ti-Mo alloys containing 2.5–10 wt% with excellent strength and toughness was fabricated from elemental powders. Using a two-stage process of spark plasma sintering and hot-extrusion, the powders were consolidated into high density materials with exceptional mechanical performance that arises from the thermo-mechanically processed microstructures. The key findings are summarised as follows:

1) Single step spark-plasma-sintering for 1 h at 1000°C was sufficient to produce fully homogeneous Ti-Mo alloys of up to 10 wt% without further post-homogenisation treatments. Elemental Mo, and Mo enriched regions were not detected by either XRD or EDS analyses.
2) XRD analysis confirmed stabilisation of the β-phase with increasing Mo addition. Both extruded α and β lattices showed progressive contraction with increasing Mo content, suggesting increasing dissolution into both lattices as substitutional solutes.
3) Mo significantly altered the microstructure development of extruded Ti in the range of 0–10 wt% addition. Progressive refinement of α-Ti grains is observed at lower additions of 2.5 wt% and 5 wt%, as the β → α transformation becomes progressively suppressed by the increased β stability. EBSD reveals almost equal fractions of α and β at 7.5 wt%, while a highly deformed β structure is completely retained at 10 wt%.
4) Across the compositions, α microstructures appear to develop through the progressive coarsening of Widmanstätten colonies in micro-textured bands with basal and prismatic poles oriented along the extrusion direction. These originate from variants of the Burgers orientation relationship derived from deformed β microstructures with strong <110> texture in the extrusion direction.
5) These microstructures produced significant improvements mechanical properties over similarly processed CP-Ti. Ti-5Mo exhibited exceptional tensile toughness with twice the strength of CP-Ti at no cost to ductility, while Ti-10Mo achieved an extraordinary strength of over 1400 MPa while maintaining an elongation of ~10 %.
6) This excellent tensile toughness appears to be enabled by a combination of solid-solution strengthening, dislocation strengthening, and grain refinement effects with a fracture resistant configuration of grains produced by thermomechanical processing. The entire series of materials vastly outperforms all other reported Ti-Mo alloys in terms of strength-ductility balance.

In combination, these findings reveal the high potential of obtaining excellent and tailorable properties from the compositionally simple, and relatively cheap Ti-Mo system. They also demonstrate the remarkable utility of thermomechanical processing in developing ultra-strong titanium alloys with excellent specific strength.

CRediT authorship contribution statement

Katsuyoshi Kondoh: Writing – review & editing, Validation, Supervision, Resources, Project administration, Methodology, Funding acquisition, Conceptualization. **Abdollah Bahador:** Writing – review & editing, Validation, Supervision, Methodology. **Jeff Huang:** Writing – original draft, Visualization, Investigation, Formal analysis, Conceptualization.

Declaration of Competing Interest

The authors declare that they have no known competing financial interests or personal relationships that could have appeared to influence the work reported in this paper.

Acknowledgements

The authors acknowledge funding from the OU Master Plan Implementation Project of Osaka University (Japan), and the Light Metal Education Foundation (Japan). The authors also gratefully thank Mr Nattawood Suesawadwanid (King Mongkut's University of Technology Thonburi, Thailand) for his contributions to data collection process, and Prof. Junko Umeda (Osaka University, Japan) for her assistance to the administration of the project.

Appendix A. Supporting information

Supplementary data associated with this article can be found in the online version at doi:10.1016/j.jallcom.2024.177195.

Data availability

Data supporting the results of this work are available from corresponding authors upon reasonable request.

References

[1] G.J. Simandl, S. Paradis, Vanadium as a critical material: economic geology with emphasis on market and the main deposit types, Appl. Earth Sci. 131 (2022) 218–236, https://doi.org/10.1080/25726838.2022.2102883.

[2] B.C. Costa, C.K. Tokuhara, L.A. Rocha, R.C. Oliveira, P.N. Lisboa-Filho, J. Costa Pessoa, Vanadium ionic species from degradation of Ti-6Al-4V metallic implants: in vitro cytotoxicity and speciation evaluation, Mater. Sci. Eng. C 96 (2019) 730–739, https://doi.org/10.1016/j.msec.2018.11.090.

[3] J.C. Williams, R.R. Boyer, Opportunities and issues in the application of titanium alloys for aerospace components, Metals 10 (2020) 705, https://doi.org/10.3390/met10060705.

[4] M.O. Bodunrin, L.H. Chown, J.A. Omotoyinbo, Development of low-cost titanium alloys: a chronicle of challenges and opportunities, Mater. Today Proc. 38 (2021) 564–569, https://doi.org/10.1016/j.matpr.2020.02.978.

[5] D. Raabe, B. Sander, M. Friák, D. Ma, J. Neugebauer, Theory-guided bottom-up design of β-titanium alloys as biomaterials based on first principles calculations: theory and experiments, Acta Mater. 55 (2007) 4475–4487, https://doi.org/10.1016/j.actamat.2007.04.024.

[6] S.S. Sidhu, H. Singh, M.A.-H. Gepreel, A review on alloy design, biological response, and strengthening of β-titanium alloys as biomaterials, Mater. Sci. Eng. C 121 (2021) 111661, https://doi.org/10.1016/j.msec.2020.111661.

[7] B. Dutta, F.H. (Sam) Froes, The Additive Manufacturing (AM) of titanium alloys, Met. Powder Rep. 72 (2017) 96–106, https://doi.org/10.1016/j.mprp.2016.12.062.

[8] F.H. Froes, M. Qian, A perspective on the future of titanium powder metallurgy, in: Titanium Powder Metallurgy, Elsevier, 2015, pp. 601–608, https://doi.org/10.1016/B978-0-12-800054-0.00031-9.

[9] D. Blanco, E.M. Rubio, R.M. Lorente-Pedreille, M.A. Sáenz-Nuño, Sustainable processes in aluminium, magnesium, and titanium alloys applied to the transport sector: a review, Metals 12 (2021) 9, https://doi.org/10.3390/met12010009.

[10] J.L. Murray, The Mo−Ti (molybdenum-titanium) system, Bull. Alloy Phase Diagr. 2 (1981) 185–192, https://doi.org/10.1007/BF02881476.

[11] B. Zhang, Z. Liu, X. Wu, D. Zhang, Sustaining an excellent strength-ductility combination of a PM α + β titanium alloy with fine prior β grains and heterogeneous microstructure, J. Alloy. Compd. 926 (2022) 166736, https://doi.org/10.1016/j.jallcom.2022.166736.

[12] S. Ehtemam-Haghighi, H. Attar, I.V. Okulov, M.S. Dargusch, D. Kent, Microstructural evolution and mechanical properties of bulk and porous low-cost Ti–Mo–Fe alloys produced by powder metallurgy, J. Alloy. Compd. 853 (2021) 156768, https://doi.org/10.1016/j.jallcom.2020.156768.

[13] Y. Abdelrhman, M.A.-H. Gepreel, S. Kobayashi, S. Okano, T. Okamoto, Biocompatibility of new low-cost (α + β)-type Ti-Mo-Fe alloys for long-term implantation, Mater. Sci. Eng: C 99 (2019) 552–562, https://doi.org/10.1016/j.msec.2019.01.133.

[14] W. Xu, M. Chen, X. Lu, D. Zhang, H. Singh, Y. Jian-shu, Y. Pan, X. Qu, C. Liu, Effects of Mo content on corrosion and tribocorrosion behaviours of Ti-Mo orthopaedic alloys fabricated by powder metallurgy, Corros. Sci. 168 (2020) 108557, https://doi.org/10.1016/j.corsci.2020.108557.

[15] G.C. Cardoso, G.S. De Almeida, D.O.G. Corrêa, W.F. Zambuzzi, M.A.R. Buzalaf, D. R.N. Correa, C.R. Grandini, Preparation and characterization of novel as-cast Ti-Mo-Nb alloys for biomedical applications, Sci. Rep. 12 (2022) 11874, https://doi.org/10.1038/s41598-022-14820-8.

[16] S.X. Liang, K.Y. Liu, Y.D. Shi, B. Zhang, R.S. Yin, L.H. Dong, H.R. Lu, M.Z. Ma, R. P. Liu, X.Y. Zhang, Microstructure evolution and mechanical properties of the Ti–Mo double harmonic alloy after annealing treatment, Mater. Sci. Eng. A 894 (2024) 146191, https://doi.org/10.1016/j.msea.2024.146191.

[17] M. Shahedi Asl, S.A. Delbari, M. Azadbeh, A. Sabahi Namini, M. Mehrabian, V.-H. Nguyen, Q.V. Le, M. Shokouhimehr, M. Mohammadi, Nanoindentational and conventional mechanical properties of spark plasma sintered Ti–Mo alloys, J. Mater. Res. Technol. 9 (2020) 10647–10658, https://doi.org/10.1016/j.jmrt.2020.07.066.

[18] H.J. Lee, J.H. Kim, C.H. Park, J.-K. Hong, J.-T. Yeom, T. Lee, S.W. Lee, Twinning-induced plasticity mechanism of α″-martensitic titanium alloy, Acta Mater. 248 (2023) 118763, https://doi.org/10.1016/j.actamat.2023.118763.

[19] X. Min, X. Chen, S. Emura, K. Tsuchiya, Mechanism of twinning-induced plasticity in β-type Ti–15Mo alloy, Scr. Mater. 69 (2013) 393–396, https://doi.org/10.1016/j.scriptamat.2013.05.027.

[20] S.L. Semiatin, An overview of the thermomechanical processing of α/β titanium alloys: current status and future research opportunities, Met. Mater. Trans. A 51 (2020) 2593–2625, https://doi.org/10.1007/s11661-020-05625-3.

[21] Z. Wang, Y. Tan, N. Li, Powder metallurgy of titanium alloys: a brief review, J. Alloy. Compd. 965 (2023) 171030, https://doi.org/10.1016/j.jallcom.2023.171030.

[22] J.L. Xu, S.C. Tao, L.Z. Bao, J.M. Luo, Y.F. Zheng, Effects of Mo contents on the microstructure, properties and cytocompatibility of the microwave sintered porous Ti-Mo alloys, Mater. Sci. Eng. C 97 (2019) 156–165, https://doi.org/10.1016/j.msec.2018.12.028.

[23] W. Cao, S.-L. Chen, F. Zhang, K. Wu, Y. Yang, Y.A. Chang, R. Schmid-Fetzer, W. A. Oates, PANDAT software with PanEngine, PanOptimizer and PanPrecipitation for multi-component phase diagram calculation and materials property simulation, Calphad 33 (2009) 328–342, https://doi.org/10.1016/j.calphad.2008.08.004.

[24] N. Doebelin, R. Kleeberg, *Profex*: a graphical user interface for the Rietveld refinement program *BGMN*, J. Appl. Crystallogr 48 (2015) 1573–1580, https://doi.org/10.1107/S1600576715014685.

[25] S. Gražulis, D. Chateigner, R.T. Downs, A.F.T. Yokochi, M. Quirós, L. Lutterotti, E. Manakova, J. Butkus, P. Moeck, A. Le Bail, Crystallography Open Database – an open-access collection of crystal structures, J. Appl. Crystallogr 42 (2009) 726–729, https://doi.org/10.1107/S0021889809016690.

[26] R.W.G. Wyckoff, Crystal Structures, second ed., 1, Interscience Publishers, New York, 1963.

[27] A. Bahador, A. Amrin, S. Kariya, A. Issariyapat, O. Gokcekaya, G. Zhao, J. Umeda, Y. Yang, M. Qian, K. Kondoh, Excellent tensile yield strength with ultrafine grain and tailored microstructure in plastically deformed Ti–Re alloys, J. Alloy. Compd. 967 (2023) 171544, https://doi.org/10.1016/j.jallcom.2023.171544.

[28] A. Bahador, S. Kariya, J. Umeda, E. Hamzah, K. Kondoh, Tailoring microstructure and properties of a superelastic Ti–Ta alloy by incorporating spark plasma sintering with thermomechanical processing, J. Mater. Eng. Perform. 28 (2019) 3012–3020, https://doi.org/10.1007/s11665-019-04061-8.

[29] M.B. Shongwe, M.M. Ramakokovhu, S. Diouf, M.O. Durowoju, B.A. Obadele, R. Sule, M.L. Lethabane, P.A. Olubambi, Effect of starting powder particle size and heating rate on spark plasma sintering of FeNi alloys, J. Alloy. Compd. 678 (2016) 241–248, https://doi.org/10.1016/j.jallcom.2016.03.270.

[30] G.B. Kale, R.V. Patil, Chemical diffusion in titanium-molybdenum system, Mater. Trans., JIM 35 (1994) 439–444, https://doi.org/10.2320/matertrans1989.35.439.

[31] G. Lütjering, J.C. Williams, Titanium, second ed., Springer, Berlin, New York, 2007.

[32] P.J. Bania, Beta titanium alloys and their role in the titanium industry, JOM 46 (1994) 16–19, https://doi.org/10.1007/BF03220742.

[33] L. Pauling, Atomic radii and interatomic distances in metals, J. Am. Chem. Soc. 69 (1947) 542–553, https://doi.org/10.1021/ja01195a024.

[34] T. Mimoto, J. Umeda, K. Kondoh, Strengthening behaviour and mechanisms of extruded powder metallurgy pure Ti materials reinforced with ubiquitous light elements, Powder Metall. 59 (2016) 223–228, https://doi.org/10.1080/00325899.2016.1148847.

[35] X. Ji, I. Gutierrez-Urrutia, S. Emura, T. Liu, T. Hara, X. Min, D. Ping, K. Tsuchiya, Twinning behavior of orthorhombic-α" martensite in a Ti-7.5Mo alloy, Sci. Technol. Adv. Mater. 20 (2019) 401–411, https://doi.org/10.1080/14686996.2019.1600201.

[36] S.I. Wright, M.M. Nowell, D.P. Field, A review of strain analysis using electron backscatter diffraction, Microsc. Microanal. 17 (2011) 316–329, https://doi.org/10.1017/S1431927611000055.

[37] S. Zhang, Y.C. Lin, D.-G. He, Y.-Q. Jiang, H.-J. Zhang, N.-F. Zeng, G.-C. Wu, M. Naseri, Correlation between plastic deformation mechanism and texture evolution of a near β-Ti alloy deformed in β region, Intermetallics 170 (2024) 108333, https://doi.org/10.1016/j.intermet.2024.108333.

[38] D.L. OuYang, M.W. Fu, S.Q. Lu, Study on the dynamic recrystallization behavior of Ti-alloy Ti–10V–2Fe–3V in β processing via experiment and simulation, Mater. Sci. Eng. A 619 (2014) 26–34, https://doi.org/10.1016/j.msea.2014.09.067.

[39] R. Dong, H. Kou, Y. Zhao, X. Zhang, L. Yang, H. Hou, Morphology characteristics of α precipitates related to the crystal defects and the strain accommodation of variant selection in a metastable β titanium alloy, J. Mater. Sci. Technol. 95 (2021) 1–9, https://doi.org/10.1016/j.jmst.2021.01.090.

[40] A.T. Churchman, The slip modes of titanium and the effect of purity on their occurrence during tensile deformation of single crystals, Proc. R. Soc. Lond. A 226 (1954) 216–226, https://doi.org/10.1098/rspa.1954.0250.

[41] S. Hémery, C. Tromas, P. Villechaise, Slip-stimulated grain boundary sliding in Ti-6Al-4 V at room temperature, Materialia 5 (2019) 100189, https://doi.org/10.1016/j.mtla.2018.100189.

[42] Y. Ohmori, K. Nakai, H. Ohtsubo, M. Tsunofuri, Formation of Widmanstätten alpha structure in a Ti–6Al–4V alloy, Mater. Trans. JIM 35 (1994) 238–246, https://doi.org/10.2320/matertrans1989.35.238.

[43] X. Gao, S. Zhang, L. Wang, K. Yang, P. Wang, H. Chen, Evolution of grain boundary α phase during cooling from β phase field in a α + β titanium alloy, Mater. Lett. 301 (2021) 130318, https://doi.org/10.1016/j.matlet.2021.130318.

[44] S. Tu, X. Ren, J. He, Z. Zhang, Stress–strain curves of metallic materials and post-necking strain hardening characterization: a review, Fatigue Fract. Eng. Mat. Struct. 43 (2020) 3–19, https://doi.org/10.1111/ffe.13134.

[45] I. Konovalenko, P. Maruschak, J. Brezinová, J. Brezina, Morphological characteristics of dimples of ductile fracture of VT23M titanium alloy and identification of dimples on fractograms of different scale, Materials 12 (2019) 2051, https://doi.org/10.3390/ma12132051.

[46] T. Suzuki, S. Takeuchi, H. Yoshinaga, Dislocation Dynamics and Plasticity, Springer Berlin Heidelberg, Berlin, Heidelberg, 1991, https://doi.org/10.1007/978-3-642-75774-7.

[47] R.B. Calhoun, D.C. Dunand, Dislocations in metal matrix composites, in: Comprehensive Composite Materials, Elsevier, 2000, pp. 27–59, https://doi.org/10.1016/B0-08-042993-9/00002-4.

[48] G.-H. Zhao, X.Z. Liang, B. Kim, P.E.J. Rivera-Díaz-del-Castillo, Modelling strengthening mechanisms in beta-type Ti alloys, Mater. Sci. Eng.: A 756 (2019) 156–160, https://doi.org/10.1016/j.msea.2019.04.027.

[49] I. Toda-Caraballo, A general formulation for solid solution hardening effect in multicomponent alloys, Scr. Mater. 127 (2017) 113–117, https://doi.org/10.1016/j.scriptamat.2016.09.009.

[50] S. Kariya, M. Fukuo, J. Umeda, K. Kondoh, Quantitative analysis on light elements solution strengthening in pure titanium sintered materials by Labusch model using experimental data, Mater. Trans. 60 (2019) 263–268, https://doi.org/10.2320/matertrans.Y-M2018849.

[51] K. Yokota, A. Bahador, K. Shitara, J. Umeda, K. Kondoh, Mechanisms of tensile strengthening and oxygen solid solution in single β-phase Ti-35 at%Ta+O alloys,

Mater. Sci. Eng.: A 802 (2021) 140677, https://doi.org/10.1016/j.msea.2020.140677.
[52] G.S. Dyakonov, S. Mironov, I.P. Semenova, R.Z. Valiev, Strengthening mechanisms and super-strength of severely deformed titanium, in: Nanocrystalline Titanium, Elsevier, 2019, pp. 123–143, https://doi.org/10.1016/B978-0-12-814599-9.00007-9.
[53] B. Qian, S.A. Mantri, S. Dasari, J. Zhang, L. Lilensten, F. Sun, P. Vermaut, R. Banerjee, F. Prima, Mechanisms underlying enhanced strength-ductility combinations in TRIP/TWIP Ti-12Mo alloy engineered via isothermal omega precipitation, Acta Mater. 245 (2023) 118619, https://doi.org/10.1016/j.actamat.2022.118619.
[54] S. Pilz, A. Hariharan, F. Günther, M. Zimmermann, A. Gebert, Influence of isothermal omega precipitation aging on deformation mechanisms and mechanical properties of a β-type Ti-Nb alloy, J. Alloy. Compd. 930 (2023) 167309, https://doi.org/10.1016/j.jallcom.2022.167309.
[55] C. Fleißner-Rieger, M.A. Tunes, C. Gammer, T. Jörg, T. Pfeifer, M. Musi, F. Mendez-Martin, H. Clemens, On the existence of orthorhombic martensite in a near-α titanium base alloy used for additive manufacturing, J. Alloy. Compd. 897 (2022) 163155, https://doi.org/10.1016/j.jallcom.2021.163155.
[56] Y.-P. Peng, C.-P. Ju, J.-H.C. Lin, Effect of heat treatment within alpha/beta dual-phase field on the structure and tensile properties of binary Ti–Mo alloys, Mater. Trans. 59 (2018) 734–740, https://doi.org/10.2320/matertrans.M2017371.
[57] N.A. Moshokoa, M.L. Raganya, R. Machaka, M.E. Makhatha, B.A. Obadele, The effect of molybdenum content on the microstructural evolution and tensile properties of as-cast Ti-Mo alloys, Mater. Today Commun. 27 (2021) 102347, https://doi.org/10.1016/j.mtcomm.2021.102347.
[58] L. Raganya, N. Moshokoa, B.A. Obadele, P.A. Olubambi, R. Machaka, Investigation of the tensile properties of heat treated Ti-Mo alloys, Mater. Today Proc. 38 (2021) 1044–1048, https://doi.org/10.1016/j.matpr.2020.05.782.
[59] K. Zhao, X. Zhou, T. Hu, Y. Li, Z. Ye, F. Zhang, M. Wang, H. Tan, Microstructure characterization and tensile properties of Ti–15Mo alloy formed by directed energy deposition, Mater. Sci. Eng.: A 858 (2022) 144103, https://doi.org/10.1016/j.msea.2022.144103.
[60] J. Peterson, A. Issariyapat, S. Kariya, J. Umeda, K. Kondoh, The mechanical and microstructural behavior of heat treated, texture-controlled Ti-10%Mo alloys manufactured by laser powder bed fusion, Mater. Sci. Eng. A 884 (2023) 145553, https://doi.org/10.1016/j.msea.2023.145553.
[61] N. Kang, X. Lin, C. Coddet, X. Wen, W. Huang, Selective laser melting of low modulus Ti-Mo alloy: α/β heterogeneous conchoidal structure, Mater. Lett. 267 (2020) 127544, https://doi.org/10.1016/j.matlet.2020.127544.
[62] N. Kang, X. Lin, M.E. Mansori, Q.Z. Wang, J.L. Lu, C. Coddet, W.D. Huang, On the effect of the thermal cycle during the directed energy deposition application to the in-situ production of a Ti-Mo alloy functionally graded structure, Addit. Manuf. 31 (2020) 100911, https://doi.org/10.1016/j.addma.2019.100911.
[63] H. Xu, Z. Li, A. Dong, H. Xing, D. Du, L. He, H.P. Peng, G. Zhu, D. Wang, B. Sun, Selective laser melting of biomedical Ti15Mo alloy: a proper combination of strength and ductility under the effects of multiple mechanisms, J. Alloy. Compd. 873 (2021) 159686, https://doi.org/10.1016/j.jallcom.2021.159686.
[64] Y.-L. Zhou, D.-M. Luo, Microstructures and mechanical properties of Ti–Mo alloys cold-rolled and heat treated, Mater. Charact. 62 (2011) 931–937, https://doi.org/10.1016/j.matchar.2011.07.010.
[65] Y.-D. Im, Y.-K. Lee, Effects of Mo concentration on recrystallization texture, deformation mechanism and mechanical properties of Ti–Mo binary alloys, J. Alloy. Compd. 821 (2020) 153508, https://doi.org/10.1016/j.jallcom.2019.153508.
[66] C.-C. Chung, S.-W. Wang, Y.-C. Chen, C.-P. Ju, J.-H. Chern Lin, Effect of cold rolling on structure and tensile properties of cast Ti–7.5Mo alloy, Mater. Sci. Eng. A 631 (2015) 52–66, https://doi.org/10.1016/j.msea.2015.02.045.